Green Chemistry

PAPER

View Article Online
View Journal | View Issue

Cite this: *Green Chem.*, 2026, **28**, 4896

Direct regeneration of hard carbon anodes from spent sodium-ion batteries *via* flash Joule heating

Bingwu Wang,†[a] Dong Xie,†[a] Han Jia,[b] Yu Yang,[a] Moqi Zhang,[a] Ying Wang,[a] Wei Ai [a] and Ke Wang *[a]

Received 21st November 2025,
Accepted 5th February 2026

DOI: 10.1039/d5gc06238a

rsc.li/greenchem

Sodium-ion batteries (SIBs), having been commercialized in 2023, are projected to achieve considerable market penetration in the future. However, owing to the strong similarity in material composition to lithium-ion batteries (LIBs), integrated recycling strategies are essential to ensure both high efficiency and a low environmental footprint. Herein, we report an efficient and environmentally friendly flash Joule heating (FJH) method for regenerating degraded hard carbon anodes. The ultrafast high-temperature treatment induces the thermal decomposition of polymer binders while simultaneously carbonizing the organic components of the solid electrolyte interphase into conductive graphitic carbon coatings and restoring the graphitic lattice order in degraded hard carbon. Notably, the regenerated hard carbon exhibits superior electrical performance relative to new commercial-grade hard carbon, featuring an initial coulombic efficiency of 81%, a reversible capacity of 292.3 mAh g^{-1} at 0.1 A g^{-1}, a capacity retention of 91% after 350 cycles, and a superb rate capability of 216.9 mAh g^{-1} at 5 A g^{-1}. These findings demonstrate the viability of FJH in the sustainable and cost-effective regeneration of degraded hard carbon anodes from SIBs.

Green foundation

1. In response to the limited lifespan and rapid growth of sodium-ion batteries, we propose a rapid, low-carbon flash Joule heating (FJH) strategy as a new generation of direct recycling technology for degraded hard carbon anodes, overcoming the high energy consumption and secondary pollution associated with conventional hydrometallurgical and pyrometallurgical routes.
2. The ultrafast high-temperature treatment decomposes polymer binders, *in situ* carbonizes solid electrolyte interphase organics into conductive graphitic coatings, and restores graphitic lattice order, thereby achieving superior electrochemical performance compared with commercial hard carbon while minimizing additional reagents, energy use, and emissions.
3. Future work should systematically integrate FJH into modular, large-scale recycling chains for both sodium- and lithium-ion batteries, clarify its implementation pathways for different feedstocks, and carry out comprehensive life-cycle and techno-economic assessments to guide industrial deployment toward greener, more efficient, and more cost-effective closed-loop battery recycling.

1. Introduction

Sodium-ion batteries (SIBs) have emerged as a promising alternative to lithium-ion batteries for large-scale energy storage applications, with the global SIB market projected to reach $4.8 billion by 2030.[1–3] Nevertheless, SIBs exhibit a constrained lifespan (2–5 years), leading to a growing volume of end-of-life batteries that pose environmental and resource challenges.[4] The recycling of spent SIBs through closed-loop material regeneration has strategic significance, addressing the issues of environmental preservation and resource sustainability. Current research on spent SIB recycling predominantly focuses on extracting strategic metals from cathode components,[5–9] with the direct regeneration of hard carbon (HC) anodes receiving inadequate attention. This research gap is particularly significant because virgin HC production demands energy-intensive pyrolysis (1000–1500 °C), emitting 3.1–5.2 tons of CO_2 per ton based on the precursor type used.[10–13] Regenerated HC achieves a 30–40% cost reduction compared to virgin material production,[14] simultaneously reducing environmental impacts and establishing closed-loop material cycles for sustainable energy storage.

Recent investigations have revealed that the degradation of HC anodes occurs through three primary mechanisms: (i) irreversible pore collapse during sodiation/desodiation cycles,[15,16]

[a]*State Key Laboratory of Flexible Electronics and Institute of Flexible Electronics (IFE), Northwestern Polytechnical University (NPU), 127 West Youyi Road, Xi'an 710129, PR China. E-mail: iamkwang@nwpu.edu.cn*
[b]*School of Electronics and Information, Northwestern Polytechnical University, 127 West Youyi Road, Xi'an, Shaanxi 710129, PR China*
† These authors contributed equally to this work.

(ii) the progressive accumulation of defects within the turbostratic carbon structure,[17–19] and (iii) uncontrolled thickening of the solid–electrolyte interphase (SEI) layer.[20–23] Accordingly, to regenerate battery-grade HC from spent materials, effective recycling processes must ensure both the comprehensive removal of contaminants and the restoration of structural integrity, along with SEI layer reconstruction.[24] Existing conventional methods, such as acid leaching and high-temperature treatment, effectively eliminate SEI and impurities from degraded HC, yet they struggle to restore its crystalline integrity.[25–28] Although surface coating modifications enhance electrical conductivity, they fail to mitigate the intrinsic structural disorder inherent in the HC matrix.[28,29] More importantly, most regeneration methods are generally complex, exhibit low efficiency, and fail to improve the performance, resulting in significant barriers in large-scale production.[30,31]

Flash Joule heating (FJH) is a direct resistive heating methodology involving the application of short-duration, high-current electrical pulses through a conductive material, rapidly inducing intense Joule heating within the material without thermal mediation.[32–35] Compared to conventional radiative heating or wet chemical methods, FJH offers significant improvements in terms of energy efficiency, processing speed, solvent-free operation, and thermal loss minimization.[36] In the field of LIB recycling, the FJH process has been primarily explored in terms of the separation and regeneration of cathode/anode active materials from spent batteries.[24,37–40] Moreover, FJH has demonstrated efficacy in the thermal treatment of black mass (*i.e.*, crushed electrode composites), with subsequent HCl leaching achieving >95% recovery rates for critical metals (*e.g.*, Li, Co, Ni, and Mn).[38,41–43] However, the recovery and structural regeneration of HC from spent SIBs *via* the FJH method remains insufficiently explored.

In this study, we present a current-regulated FJH method coupled with HCl leaching to efficiently convert degraded HC of spent SIBs into high-performance battery-grade anode materials. The rapid electrothermal process achieves temperatures exceeding 2100 K with ultrahigh heating/cooling rates ($>10^4$ K s^{-1}), enabling the complete pyrolysis of polymer binders while simultaneously carbonizing SEI organic components into conductive graphitic coatings and restoring graphitic order in degraded HC. Additional decomposition byproducts consist of inorganic salts (*e.g.*, Na_2CO_3 and Na_2O) that can be effectively recovered through 0.1 M HCl treatment. The regenerated HC demonstrates exceptional electrochemical performance, featuring an initial coulombic efficiency (ICE) of 81%, a reversible capacity of 292.3 mAh g^{-1} at 0.1 A g^{-1}, a capacity retention of 91% after 350 cycles in DME, and a superb rate capability of 216.9 mAh g^{-1} at 5 A g^{-1}. Our research develops an innovative FJH strategy that achieves the simultaneous reutilization of degraded HC anodes. This approach further provides mechanistic insights into how high-temperature treatment restores electrochemical performance through surface defect reconstruction and crystallographic reorientation.

2. Experimental section

2.1. Separation and collection of degraded hard carbon anode sheets

Cylindrical 18650-format sodium-ion batteries with a rate capacity of 1300 mAh were obtained from Jiangsu Transimage Technology Co., Ltd. These cells were subjected to continuous charge–discharge cycling at a current density of 1 C until their residual capacity declined to approximately 70% of the initial value. Following capacity fading, all disassembly procedures were carried out under an inert argon atmosphere within a glovebox. The cells were opened, and the anode foils were manually extracted. The residual degraded hard carbon (D-HC) was carefully scraped from the anode surface. The collected powder was promptly transferred, under continuous inert gas protection, into a quartz tube with graphite electrodes on both ends, in preparation for flash Joule heating regeneration.

2.2. Joule heating regeneration and subsequent purification

The flash Joule heating regeneration process was conducted in a quartz tube with an inner diameter, outer diameter, and length of 10 cm, 14 cm, and 50 cm, respectively. The entire flash heating apparatus was self-assembled, forming a closed circuit *via* a capacitor with a capacitance of 90 mF. During the regeneration process, the heating rate reached approximately 2.5×10^4 K s^{-1}. Upon reaching a peak temperature of ~2190 K, the material was rapidly cooled at a rate of $\sim 3.6 \times 10^4$ K s^{-1}. The total duration of the regeneration process was less than 0.2 s. A voltage of 130 V was applied during the process, and the peak current in the circuit reached up to 220 A. The resulting materials were denoted as FR-HC (Flash-Regenerated Hard Carbon).

To highlight the advantages of flash Joule heating over conventional calcination in hard carbon regeneration, the same D-HC sample was subjected to traditional thermal treatment in a tube furnace. The sample was heated to 1100 °C at a rate of 5 °C min^{-1}, held at this temperature for 1 hour, and then naturally cooled to room temperature to obtain CR-HC (calcined regenerated hard carbon). Both regenerated samples were further purified by soaking in 0.1 M hydrochloric acid solution for 24 hours to remove residual impurities.

2.3. Material characterization

X-ray diffraction (XRD) analysis was carried out using a Bruker D8 Advance diffractometer with Cu Kα radiation (λ = 1.54056 Å) to examine the phase composition and crystalline structure of the samples. Surface chemical compositions were assessed by X-ray photoelectron spectroscopy (XPS) using an ESCALab MKII instrument with an Al Kα excitation source. Specific surface areas were determined by the Brunauer–Emmett–Teller (BET) method, and pore structure characteristics were derived using non-local density functional theory (NLDFT) analysis. Small-angle X-ray scattering (SAXS) was carried out using an Anton Paar Saxesess mc2 system operated at 40 kV and 50 mA. The surface morphology was observed using a ZEISS Gemini SEM 300 at 3 kV, and detailed micro-

structural features were imaged using an FEI Talos F200X transmission electron microscope (TEM) at 200 kV. Fourier-transform infrared (FTIR) spectra were recorded using a Bruker TENSOR 27 spectrometer, and thermal stability was assessed by thermogravimetric analysis (TGA) using a NETZSCH STA 449F3 instrument, in which samples were heated from room temperature to 1000 °C at 10 °C min^{-1} under a nitrogen atmosphere. Raman spectra were recorded with a Renishaw inVia system using a 532 nm laser, and UV-vis absorption measurements were performed using a U3900H spectrophotometer.

2.4. Electrochemical measurements

Electrochemical performance was evaluated using CR2032-type coin cells. Working electrodes were fabricated by mixing the active hard carbon material with Super P conductive carbon and PVDF binder in a weight ratio of 8 : 1 : 1, using *N*-methyl-2-pyrrolidone (NMP) as the dispersant. The homogeneous slurry was coated onto copper foil and dried under vacuum at 80 °C for 12 hours. The dried electrodes were then punched into 12 mm diameter disks. Half-cell assembly was conducted in an argon-filled glovebox (H_2O and O_2 <0.1 ppm), employing sodium metal as both counter and reference electrodes. A Whatman GF/D glass microfiber membrane was used as the separator, and the electrolyte was composed of 1 M $NaPF_6$ dissolved in either dimethyl ether (DME) or diethyl carbonate (DEC), corresponding to ether- and ester-based systems, respectively. For full-cell configurations, the cathode was prepared using $NaNi_{1/3}Fe_{1/3}Mn_{1/3}O_2$, conductive carbon, and PVDF in the same 8 : 1 : 1 mass ratio. Electrochemical tests included galvanostatic charge–discharge (GCD) and galvanostatic intermittent titration technique (GITT), carried out using a Neware multichannel battery tester within a voltage range of 0.01–3.00 V (*vs.* Na^+/Na). Cyclic voltammetry (CV) was performed using a CHI760E electrochemical workstation, while electrochemical impedance spectroscopy (EIS) was recorded over a frequency range of 100 kHz to 0.01 Hz using an Autolab instrument under open-circuit conditions.

3. Results and discussion

As shown in Fig. 1a, degraded hard carbon (D-HC) exhibits a surface-proximal defective SEI characterized by nanoscale

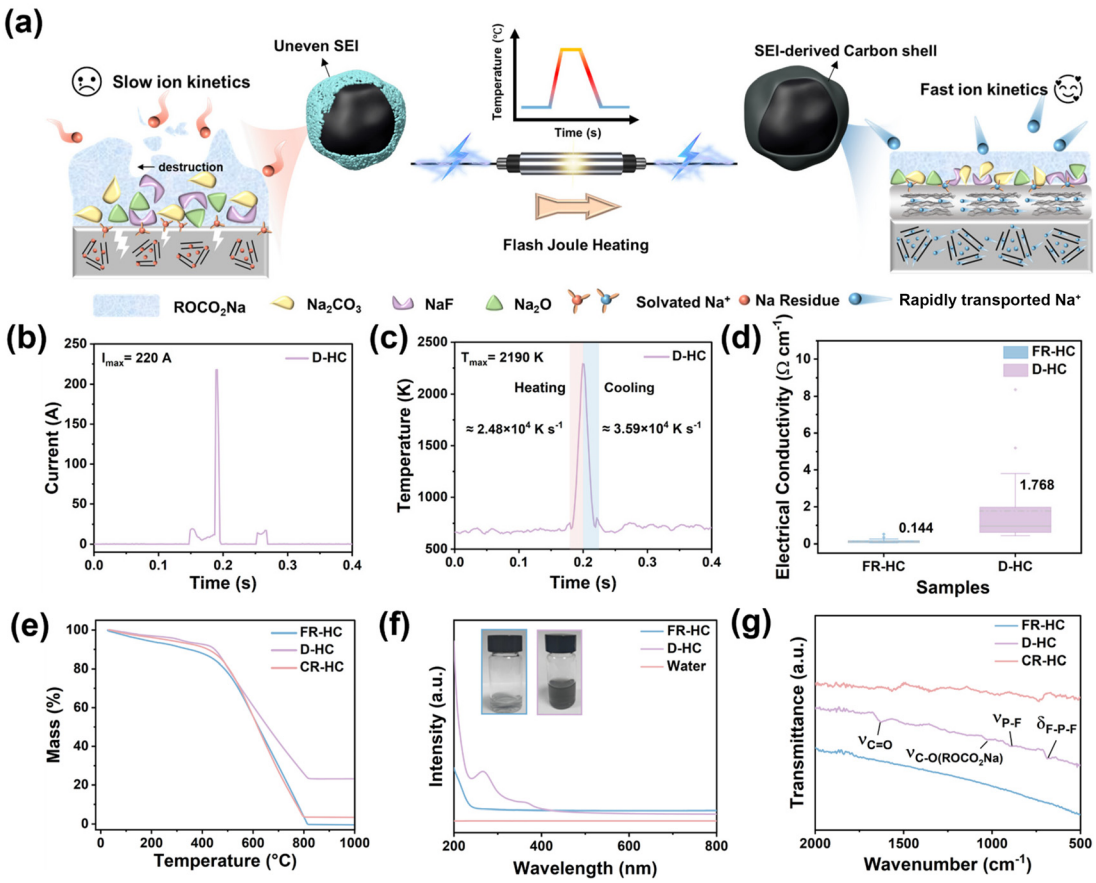

Fig. 1 (a) Schematic of the FJH regeneration process. (b) Corresponding current–time curve during the FJH process. (c) Corresponding temperature–time curve during the FJH process. (d) Thin-film conductivity of FR-HC and D-HC. (e) TGA thermogram of different HC samples. (f) UV-vis spectra of the water leaching solutions from FR-HC and D-HC. Optical images show the black and transparent solutions derived from D-HC (purple frame) and FR-HC (blue frame), respectively. (g) FTIR spectra of FR-HC, CR-HC, and D-HC.

lattice imperfections, indicative of progressive structural degradation during extended cycling. This degradation not only triggers irreversible sodium inventory loss through parasitic reactions but also induces abnormal inhomogeneous SEI thickening dominated by organic–inorganic hybrid components (*e.g.*, $ROCO_2Na$, Na_2O, NaF, and Na_2CO_3).[23,44] The organic-rich SEI imposes kinetic barriers to Na^+ desolvation, intensifying interfacial polarization and resulting in reduced ICE and rate performance.[45] This study introduces the FJH regeneration method, where an ultra-rapid electrothermal process (>10^4 K s^{-1} heating/cooling rates, >2100 K) achieves complete binder pyrolysis while converting SEI organics into conductive graphitic coatings and restoring graphitic order in degraded HC. The reconstructed architecture features aligned graphite microcrystals that shorten Na^+ diffusion paths and accelerate ion kinetics, enabling the regenerated HC (FR-HC) to form an inorganic-rich SEI layer for facilitated desolvation and enhanced ICE/rate performance. During FJH treatment, D-HC powders were exposed to pulsed currents (peak amplitude: 220 A, pulse width: 50 ms) under an argon atmosphere, powered by a 90 mF capacitor charged to 130 V (Fig. 1b). Time-resolved pyrometry recorded ultrafast thermal transients with a peak temperature of 2190 K, alongside heating and cooling rates of 2.50 × 10^4 K s^{-1} and 3.59 × 10^4 K s^{-1}, respectively (Fig. 1c). Post-treatment resistivity measurements decreased 12-fold from 1.768 to 0.144 Ω cm^{-1} due to the reductive elimination of insulating contaminants, accompanied by enhanced graphitization and formation of short-range ordered, π-conjugated domains, synergistically improving the conductivity (Fig. 1d).[46]

To assess the efficiency of impurity removal by the FJH regeneration process, thermogravimetric analysis (TGA) was conducted under an air atmosphere (Fig. 1e). All HC samples exhibit identical pyrolysis behavior between 20 °C and 500 °C, showing nearly a similar mass-loss trend, which can be ascribed to the volatilization of physically adsorbed water and organic components within the SEI layer (*e.g.*, $ROCO_2Na$ and RONa). In the temperature range of 500–800 °C, all three samples exhibit a rapid mass decrease, which is attributed to the oxidation of carbonaceous frameworks. Notably, the mass-loss rate of D-HC is markedly lower than those of FR-HC and CR-HC, owing to the presence of thermally stable components within the thick SEI layer (*e.g.*, Na_2O and Na_2CO_3) that retard the oxidation process. At elevated temperatures above 800 °C, D-HC and CR-HC retain significant residual masses (~26.1% and ~4.2%), indicating the presence of thermally stable inorganic residues, including dead sodium and cathode-derived metal oxides. By contrast, FR-HC undergoes nearly complete combustion with negligible residue, thereby confirming the superior efficiency of the FJH regeneration process in eliminating SEI layers, inactive metallic species, and oxide contaminants.

UV-vis and Fourier-transform infrared (FTIR) spectroscopy methods were employed to further elucidate the functional compositions of the SEI and residual electrolyte species. The UV-vis spectrum of aqueous D-HC leachates revealed a broad absorption band at ≈220 nm (Fig. 1f), which can be assigned to soluble carbonate species and residual electrolyte components. Conversely, the supernatant of FR-HC exhibited no discernible absorption features, confirming the effective removal of organic impurities. In the FTIR spectra of D-HC and CR-HC, distinct absorption bands are observed at ≈1632 and ≈1040 cm^{-1}, corresponding to C═O stretching ($\nu_{C=O}$) and C–O stretching (ν_{C-O}) vibrations, respectively, indicative of SEI organic compounds and surface oxygenated groups. Additional bands at ≈837 cm^{-1} (ν_{P-F}) and ≈687 cm^{-1} (δ_{P-F}) are attributed to electrolyte decomposition products (Fig. 1g). Notably, these characteristic features are absent in the FTIR spectrum of FR-HC, highlighting the efficacy of FJH treatment in eliminating both SEI-related organics and residual electrolyte impurities.

The structural evolution of carbon during regeneration was elucidated by X-ray diffraction (XRD) and Raman spectroscopy (Fig. 2a and b). All HC samples exhibit two broad peaks at ≈23.5° and ≈43.5°, indexed to the (002) and (100) planes of turbostratic carbon, suggesting the preservation of an amorphous-dominated framework. The interlayer spacing (d_{002}), crystallite width (L_a), and stacking height (L_c) were quantified using Bragg's law and the Scherrer equation (Fig. S1a and b). HC shows d_{002} ≈ 0.38 nm with L_a ≈ 14.5 nm and L_c ≈ 2.0 nm, typical of a disordered carbon structure. After extensive cycling, D-HC exhibits obvious broadening and a left shift of the (002) peak, corresponding to an enlarged d_{002} (≈0.44 nm) and decreased L_a (≈12.3 nm) and L_c (≈1.4 nm), indicative of lattice expansion and microcrystal fragmentation arising from repetitive Na^+ intercalation and dead-sodium trapping. Upon conventional annealing, CR-HC largely restores the (002) reflection to ≈0.38 nm while showing a modest increase in L_a and L_c, reflecting partial graphitization and limited defect recovery. In contrast, FR-HC displays the sharpest (002) peak with a slightly contracted d_{002} (≈0.37 nm) and markedly enlarged L_a (≈15.6 nm) and L_c (≈2.7 nm), confirming that the ultrafast, ultra-high-temperature FJH process enables efficient graphitic reconstruction and long-range ordering. Raman spectroscopy further elucidates the defect evolution and structural reorganization of the regenerated HCs. All samples show two characteristic bands, namely the D band (≈1350 cm^{-1}) and the G band (≈1580 cm^{-1}), corresponding to structural defects and sp^2 carbon vibrations, respectively. The defect concentration is typically evaluated by the intensity ratio of the D and G bands (I_D/I_G). Compared to HC, the I_D/I_G ratio of D-HC increases from 0.99 to 1.06, indicating defect accumulation due to repetitive Na^+ intercalation and inactive sodium deposition. CR-HC shows a reduced I_D/I_G value of ≈0.90, suggesting partial recovery of graphitic order through defect healing. Strikingly, FR-HC presents the lowest I_D/I_G (≈0.77) along with an intensified 2D band (≈2700 cm^{-1}), characteristic of graphitic stacking, signifying extensive lattice reordering and enhanced graphitization triggered by the ultrafast FJH process.[47] The substantial reduction in I_D/I_G suggests that the ultrafast FJH treatment promotes rapid structural reorganization and a lower density of disorder/defect sites in the carbon matrix. Meanwhile, the G-band narrowing together with the more pro-

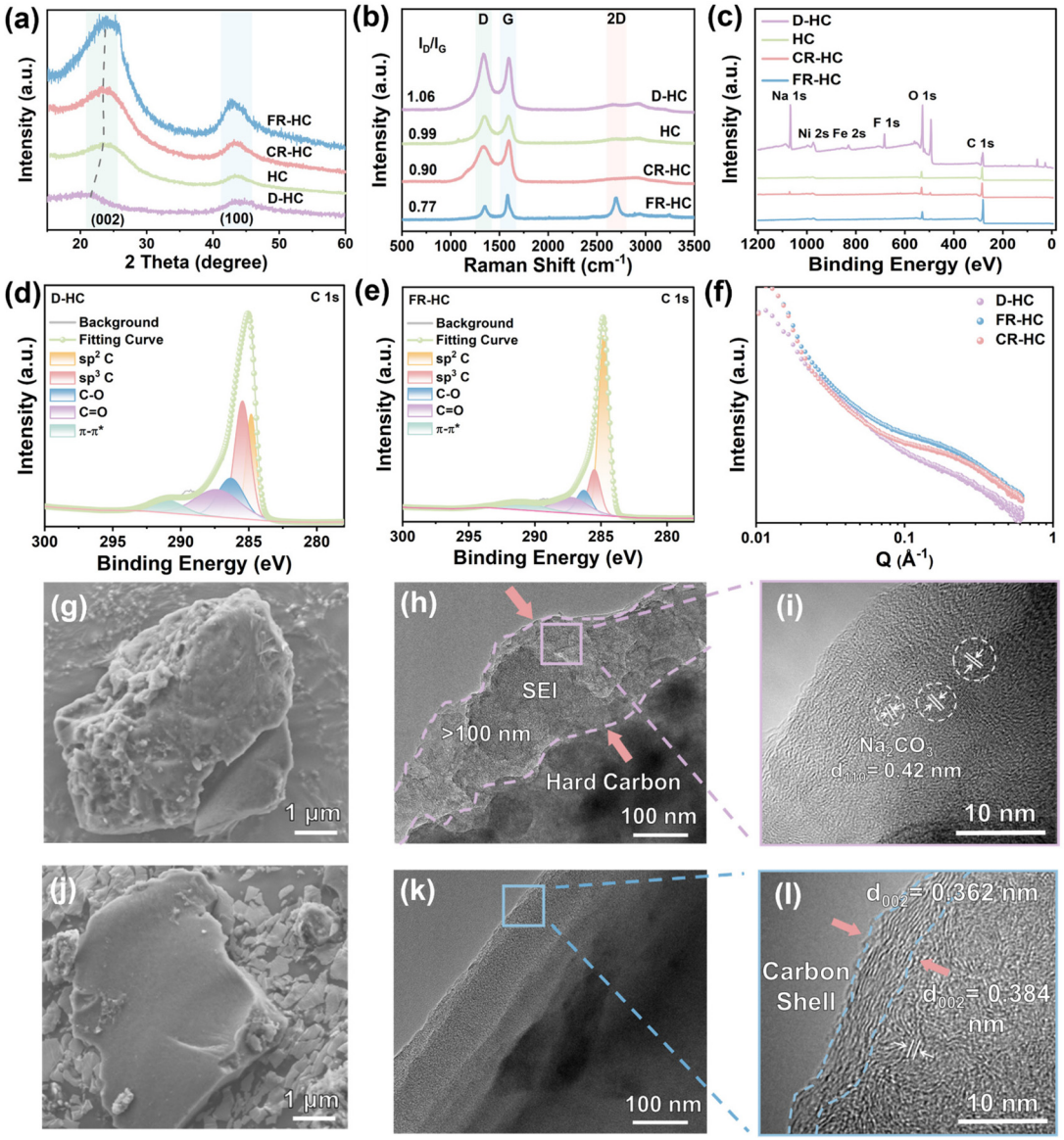

Fig. 2 (a) XRD patterns of FR-HC, CR-HC, HC, and D-HC. (b) Raman spectra of D-HC, HC, CR-HC and FR-HC. (c) XPS spectra of D-HC, HC, CR-HC and FR-HC. (d and e) C 1s spectra of D-HC and FR-HC. (f) SAXS patterns of D-HC, FR-HC and CR-HC. (g and j) SEM images of D-HC and FR-HC. (h and k) TEM images of D-HC and FR-HC. (i and l) HR-TEM images of D-HC and FR-HC.

nounced 2D band for FR-HC points to increased sp^2 ordering and improved stacking order. In line with the XRD results (reduced d_{002} and enlarged L_a/L_c), the Raman features collectively support the conclusion that FJH enables efficient defect healing and graphitic domain reconstruction.[48]

The chemical content and bonding configuration of HCs were determined using X-ray photoelectron spectroscopy (XPS) (Fig. 2c). D-HC retained a C content of 47.18%, an O content of 40.89%, and a Na content of 11.84%, along with trace F and transition-metal residues (Ni and Fe) originating from cathode dissolution. These species are likely associated with surface residues and impurities introduced during cell operation (*e.g.*, possibly from cathode dissolution, current collectors, or cell manufacturing components). After high-temperature annealing, CR-HC contains a C content of 83.54%, accompanied by a certain reduction in O content (14.00%) and residual Na content (2.46%), implying that conventional thermal treatment is insufficient to fully remove oxygenated defects and trapped sodium species in bulk carbon. Notably, FR-HC exhibits a pronounced reduction in the O content with a value of 10.91% and a high C proportion of 89.09%, with no impurity signals observed above the XPS detection limit, confirming the high effectiveness of the FJH regeneration process in impurity mitigation. The deconvolution of the C 1s spectra reveals that D-HC contains 19.43% sp^2 carbon and 33.04% sp^3 carbon (Fig. 2d). Meanwhile, FR-HC exhibits a markedly higher sp^2 contribution of 52.29% along with a reduced sp^3 fraction of 15.24% (Fig. 2e and Fig. S2). Such bonding evolution suggests

the formation of more extended sp^2-hybridized domains in FR-HC, indicating a higher degree of structural ordering within the carbon matrix.

Characterizing the pore structure is critical to elucidating the sodium storage behavior of HC. N_2 adsorption/desorption analysis (Fig. S6a) revealed that D-HC exhibited a high specific surface area (37.1 m^2 g^{-1}), 36% higher than that of HC (27.2 m^2 g^{-1}), which can be ascribed to the generation of abundant structural defects induced by repeated Na^+ insertion/extraction during cycling. Through the remediation of surface defects by the FJH process, FR-HC exhibited a reduced surface area of 10.2 m^2 g^{-1}. The pore size distribution (Fig. S6b) showed that FR-HC exhibited an ultramicroporous network (1.2–1.8 nm), matching the solvated Na^+ diameter (~1.6 nm) while excluding larger PF_6^- anions (~2.1 nm). Such pore-size selectivity enables preferential Na^+ transport and effectively suppresses parasitic electrolyte decomposition, thereby stabilizing the electrode/electrolyte interface.[49] The closed-pore architectures of D-HC, FR-HC, and CR-HC were investigated by small-angle X-ray scattering (SAXS) to elucidate the structural evolution of nanopores under transient high-temperature pulses. As depicted in Fig. 2f, all HC samples exhibit a characteristic broad scattering maximum at $q \approx 0.1$–1 $Å^{-1}$, signifying the presence of closed pores in HCs. D-HC shows attenuated closed-pore signatures due to pore blocking by trapped sodium species within the carbon matrix. CR-HC exhibits a moderate increase in closed-pore intensity, suggesting that high-temperature annealing facilitates the curling and closure of partial graphitic microcrystals. In contrast, FR-HC displays the strongest scattering intensity in the intermediate q range, indicating the formation of abundant closed pores. This enhancement highlights the advantage of FJH over conventional thermal treatment in reconstructing the porous architecture. The ultrafast Joule heating treatment likely causes rapid decomposition of SEI species and carbonaceous residues, accompanied by localized gas release. These non-equilibrium conditions promote structural reconstruction of the carbon matrix, giving rise to enriched closed-pore architectures as evidenced by SAXS. Concurrently, BET analysis reveals the formation of ultramicropores with confined dimensions, which may contribute to regulated Na^+ transport and mitigated parasitic electrolyte decomposition.[50,51]

The morphological evolution of D-HC, FR-HC, and CR-HC was examined by scanning electron microscopy (SEM). As shown in Fig. 2g, j and Fig. S7, particle size statistics based on 40 particles per sample reveal distinct morphological evolutions after different regeneration treatments. D-HC exhibits pronounced particle expansion with an average diameter of ≈10.9 μm, which can be ascribed to Na^+ de/intercalation-induced lattice dilation and thick SEI accumulation upon cycling. Although CR-HC displays reduced particle size (6.8 μm) and partial structural recovery, its roughened surface with more accessible pores facilitates electrolyte infiltration and irreversible decomposition, ultimately resulting in a lower ICE and inferior cycling stability.[52] By comparison, FR-HC displays a compact morphology with markedly suppressed macroporosity, originating from the ultrafast carbon rearrangement and curling closure of graphitic layers induced by the FJH pulse reaction. Moreover, the disappearance of binder-induced agglomeration in FR-HC further evidences the self-purifying effect of FJH. Collectively, these results demonstrate that FJH synergistically promotes impurity volatilization and microstructural reconstruction, thus mitigating irreversible side reactions and enhancing electrochemical reversibility.

Transmission electron microscopy (TEM) further reveals pronounced microstructural distinctions between D-HC and FR-HC (Fig. 2h–l). D-HC particles are encapsulated by a thick and heterogeneous SEI layer exceeding 100 nm, consistent with the extensive electrolyte decomposition during long-term cycling. High-resolution TEM (HRTEM) further identifies crystalline Na_2CO_3 as the dominant component of this layer, as evidenced by distinct (110) lattice fringes (Fig. 2i). Such electrically insulating deposits hinder Na^+ desolvation and promote surface plating, accounting for the inferior electrochemical reversibility of D-HC.[53] In sharp contrast, FR-HC develops a uniform and conformal graphitic coating formed *via* FJH-induced carbonization of SEI-derived organics. This reconstructed shell exhibits an interlayer spacing of ≈0.372 nm, which lies within the optimal 0.36–0.40 nm range for Na^+ intercalation (Fig. 2k and l).[54] The formation of this graphitic interface accelerates interfacial ion transport and heals surface defects, thereby improving both the ICE and rate capability. Notably, the internal graphitic domains retain a spacing of ≈0.384 nm, suggesting that the ultrafast thermal pulse during FJH selectively restructures the surface carbon layers while preserving the bulk amorphous carbon matrix. Such surface-localized graphitization, driven by rapid thermal contraction, highlights the capability of FJH to optimize interfacial ion transport without compromising the intrinsic microstructure of HC.[24,47]

To clarify the influence of FJH regeneration on electrochemical performance, initial galvanostatic charge/discharge (GCD) of all HC samples is evaluated at 0.05 A g^{-1} featuring a slope region above 0.1 V and a plateau region below 0.1 V (Fig. 3a). FR-HC delivers a reversible discharge capacity of 379.4 mAh g^{-1} with a markedly higher ICE of 81%, compared with HC (435.0 mAh g^{-1}, 66%) and CR-HC (365.3 mAh g^{-1}, 67%). It has been reported that the decomposition of solution constituents (solvent and salt species), accompanied by SEI growth, occurs within 0.5–1.5 V (*vs.* Na/Na^+). In this voltage window, FR-HC delivers a smaller capacity contribution (45.2 mAh g^{-1}) than CR-HC (64.4 mAh g^{-1}) and HC (51.8 mAh g^{-1}), indicating more effectively suppressed SEI overgrowth and parasitic reactions. Moreover, the FJH process induces closed-pore formation and graphitic microcrystal reconstruction, which collectively reduce electrolyte accessibility and active defect sites, thereby suppressing irreversible sodium consumption and further enhancing the ICE. The corresponding slope and plateau capacities based on five individual samples were calculated and are displayed in Fig. 3b. FR-HC delivers the highest plateau capacity of 165.7 mAh g^{-1}, relative to HC (138.4 mAh g^{-1}) and CR-HC (118.2 mAh g^{-1}), resulting

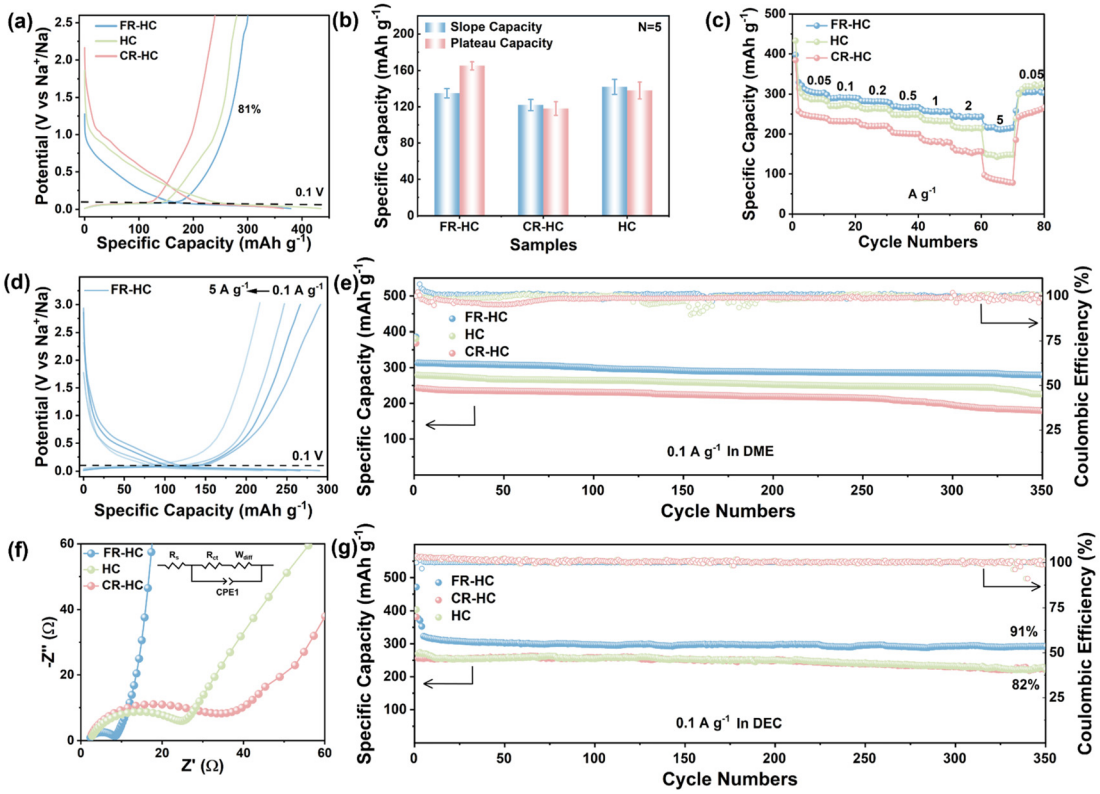

Fig. 3 (a) Initial charge–discharge profiles of FR-HC, CR-HC, and HC at 0.05 A g^{-1}. (b) Statistical analysis of the plateau capacity (N = 5). (c) Rate performance of all HC samples. (d) Voltage profiles of FR-HC at various current densities. (e) Cycling performance in an ether-based electrolyte. (f) Nyquist plots of all HC electrodes. (g) Cycling performance in an ester-based electrolyte.

from the SEI-derived graphite coatings and rich closed-pore structures.

To gain insight into the impact of the transient high-temperature treatment on fast charging performance, the rate capabilities of FR-HC, CR-HC, and HC were examined at current densities ranging from 0.05 to 5 A g^{-1}. As illustrated in Fig. 3c, FR-HC displays substantially higher reversible capacities than CR-HC and HC across the entire current-density range, which are 305.6, 292.0, 281.8, 267.5, 257.7, 246.1, and 216.9 mAh g^{-1} at current densities of 0.05, 0.1, 0.2, 0.5, 1.0, 2.0, and 5.0 A g^{-1}, respectively. Even at 5 A g^{-1}, FR-HC retains 71% of its initial capacity, whereas HC and CR-HC retain only 46% and 31%, respectively (Fig. S9). Notably, when the current density is returned to 0.05 A g^{-1}, the capacity nearly fully recovers to ~97% of the initial value. Furthermore, the voltage profiles of FR-HC and HC at different rates are shown in Fig. 3d and Fig. S10. At 5 A g^{-1}, FR-HC delivers a plateau capacity of 130.8 mAh g^{-1}, approximately two-fold higher than those of HC (59.3 mAh g^{-1}) and CR-HC (35.5 mAh g^{-1}). This outstanding rate performance is ascribed to the SEI-derived graphitic carbon shell, which accelerates Na^+ transport across the interface by forming continuous diffusion pathways that promote rapid ion kinetics. Meanwhile, the closed-pore architecture provides confined storage domains and mitigates electrolyte decomposition, collectively ensuring a high and stable plateau capacity even under high-rate conditions.

To elucidate the influence of the optimized architecture formed *via* the FJH process on cycling performance, the cycling stability was systematically assessed in $NaPF_6$/DME and $NaPF_6$/DEC electrolytes. In a DME-based electrolyte (Fig. 3e), FR-HC retains a reversible capacity of 279.3 mAh g^{-1} and an outstanding capacity retention of 89.3% after 350 cycles, which is higher than those of HC (225.9 mAh g^{-1}, 81.1%) and CR-HC (179.9 mAh g^{-1}, 74.2%). The superior performance manifests the fast Na^+ extraction capability of FR-HC, providing evidence of an SEI-derived carbon shell with optimized interlayer spacing and refined closed pores in boosting ion transport dynamics. Notably, in a DEC-based electrolyte (Fig. 3g), FR-HC delivers ultrahigh cycling stability, retaining a specific capacity of 292.3 mAh g^{-1} with an excellent capacity retention of 91% compared with HC (222.0 mAh g^{-1}, 81.5%) and CR-HC (228.6 mAh g^{-1}, 81.7%). The well-developed ultramicroporous structure of FR-HC enhances durability by molecularly sieving ester solvents to suppress infiltration and decomposition, thereby minimizing electrolyte consumption and parasitic reactions, demonstrating its viability for commercial applications.

To further examine the sodiation dynamics at the electrode/electrolyte interface, electrochemical impedance spectroscopy (EIS) was performed, as shown in Fig. 3f. The Nyquist plots are characterized by a semicircle representing charge transfer

impedance (R_{ct}) and a straight line related to ion diffusion (W_{diff}). FR-HC exhibits the lowest R_{ct} (9.3 Ω) compared with HC (22.1 Ω) and CR-HC (38.4 Ω), indicating enhanced surface graphitization (Fig. 2l) and preserved bulk crystallinity, substantiating improved Na^+ diffusion kinetics. Nevertheless, CR-HC exhibited the highest R_{ct} value, originating from incomplete defect remediation and side reactions induced by the prolonged regeneration process. These findings further highlight the efficacy of the FJH treatment in the removal of impurities and carbon phase revolution.

Cyclic voltammetry (CV) was performed within the potential range of 0.01–3.0 V (*vs.* Na/Na^+) to investigate the initial sodiation behavior of FR-HC and HC. As shown in Fig. 4a, FR-HC exhibits a distinct cathodic peak centered at 0.68 V during the first cycle, corresponding to the formation of a stable SEI layer and Na^+ intercalation into the carbon matrix. In contrast, HC presents a broader and irreversible reduction feature extending from 0.1 to 0.7 V (Fig. S11), indicative of severe electrolyte decomposition and Na^+ trapping. Moreover, the subsequent CV curves of FR-HC show well-overlapped profiles with reduced polarization, demonstrating enhanced reversibility and suppressed parasitic reactions, which ultimately contribute to 15% improvement in ICE. To gain deeper insights into the Na^+ storage kinetics, CV measurements were conducted at scan rates ranging from 0.5 to 5.0 mV s^{-1} (Fig. 4b). With increasing scan rate, the redox peaks gradually broaden while their positions remain nearly unchanged, indicating well-preserved reaction reversibility and the coexistence of diffusion-controlled and surface-capacitive processes. The relationship between the peak current (i_p) and scan rate (ν) follows the power-law equation $i_p = a\nu^b$, where the b value reflects the charge-storage mechanism. Linear fitting of the anodic and cathodic peaks yields b values of 0.44 and 0.51 for FR-HC (Fig. 4c), which are close to 0.5, indicating that Na^+ storage is primarily governed by diffusion-controlled intercalation with limited pseudocapacitive involvement. Further kinetic deconvolution using $i(V) = k_1\nu + k_2\nu^{1/2}$ reveals that the capacitive contribution of FR-HC increases from 29% at 0.2 mV s^{-1} to 60% at 5.0 mV s^{-1} (Fig. 4d). Notably, even at the highest scan rate, FR-HC retains a substantial diffusion-controlled fraction (40%), whereas HC and CR-HC exhibit 8% and 5%, respectively, demonstrating its superior Na^+ transport capability. Such diffusion persistence originates from the FJH-induced graphitic domains that shorten Na^+ migration pathways and provide continuous diffusion networks.

The galvanostatic intermittent titration technique (GITT) was employed to quantitatively analyze the Na^+ diffusion kinetics within different potential regions (Fig. 4e). The Na^+

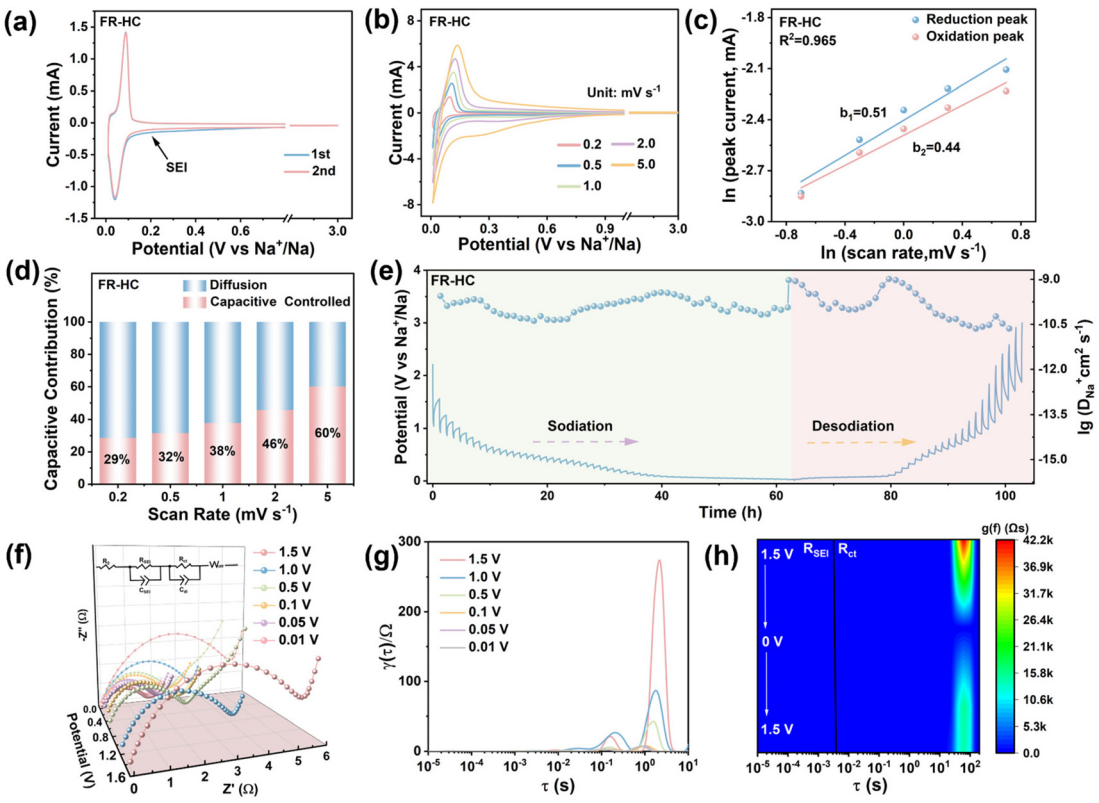

Fig. 4 (a) Cyclic voltammetry (CV) profiles of FR-HC at a scan rate of 0.1 mV s^{-1}. (b) CV profiles of FR-HC at scan rates ranging from 0.2 to 5.0 mV s^{-1}. (c) Correlation between the scan rate (ν) and peak current (i), based on oxidation and reduction peaks. (d) Capacitive *versus* diffusion-controlled contributions at various scan rates. (e) Galvanostatic intermittent titration technique (GITT) profiles during sodiation/desodiation and the corresponding Na^+ diffusion coefficients. (f) Nyquist plots of FR-HC at different discharge potentials. (g) Fitted distribution of relaxation time (DRT) curves during discharge. (h) *In situ* EIS-derived DRT transformation during the discharge process.

diffusion coefficient (D_{Na^+}) was determined using a modified form of Fick's second law:

$$D_{Na^+} = \frac{4}{\pi\tau}\left(\frac{m_B V_m}{M_B S}\right)^2\left(\frac{\Delta E_s}{\Delta E_\tau}\right)^2\left(\tau \ll \frac{L^2}{D}\right)^0$$

where m_B, V_m, M_B, and S represent the active material mass (g), molar volume ($cm^3\ mol^{-1}$), molar mass ($g\ mol^{-1}$), and electrode surface area (cm^2), respectively. In the high-potential region (1.0–0.1 V *vs.* Na/Na^+), FR-HC exhibits D_{Na^+} values in the range of 10^{-10}–10^{-9} $cm^2\ s^{-1}$, which is 10-fold higher than those of HC (10^{-11}–10^{-10} $cm^2\ s^{-1}$). This enhancement suggests that the SEI-derived graphitic coatings effectively mitigate defect-induced diffusion barriers and suppress the "trap effect" at defective sites, thereby reducing the consumption of active sodium during SEI formation. At low potentials (0.1–0.01 V), the Na^+ storage process is predominantly governed by pseudocapacitive adsorption and pore-filling behavior, leading to a gradual decrease in D_{Na^+}. Nevertheless, FR-HC maintains a diffusion coefficient significantly higher than that of HC ($\sim 10^{-9}$ *vs.* $\sim 10^{-10}$ $cm^2\ s^{-1}$) in the plateau region. This superior diffusivity is ascribed to SEI-derived conductive carbon networks that shorten Na^+ migration pathways and facilitate the transport of ions from graphitic domains to closed pores, thereby accounting for the enhanced plateau capacity of FR-HC.[55]

To gain further insights into the Na^+ (de)intercalation mechanism, *in situ* EIS combined with the distribution of relaxation times (DRT) analysis was conducted (Fig. 4f and Fig. S14a). The DRT spectra resolved three representative electrochemical processes distinguished by their time constants (τ): Na^+ permeation across the solid electrolyte interphase (SEI) ($\tau < 0.1$ s, R_{SEI}), charge transfer reaction at the electrode–electrolyte interface (0.1 s $< \tau <$ 10 s, R_{ct}), and solid-state diffusion of Na^+ in the bulk phase ($\tau > 10$ s).[56,57] Compared with HC, FR-HC exhibited a leftward shift in the τ-distribution within the R_{ct} region, indicating improved Na^+ extraction kinetics and correlating with its enhanced ICE (81% *vs.* 67% for HC). Quantitative fitting further showed that the R_{ct} value of FR-HC (9.3 Ω) was significantly reduced by 58% compared to that of HC (22.1 Ω), which can be ascribed to graphitic surface passivation that suppresses polarization induced by surface defects (Fig. 4g and Fig. S14b). During the initial sodiation process (1.2–0.6 V), the formation of an SEI resulted in an increase in R_{ct}. As the potential decreased below 0.1 V, FR-HC exhibited a marked reduction in R_{ct}, reaching a minimum of 0.8 Ω at 0.01 V. This behavior indicates the completion of Na^+ intercalation into pseudo-graphitic domains (d_{002} = 0.372 nm) and the establishment of a stable SEI layer. In contrast, HC exhibited a consistently higher R_{ct} during the desodiation process, which may be attributed to the formation of a thicker SEI layer and residual surface defects generated during the preceding sodiation step. Notably, FR-HC maintained a more reversible R_{ct} evolution throughout the cycling process, highlighting its superior interfacial stability enabled by the graphitic coating structure.

Depth-resolved XPS analysis with Ar^+ sputtering was conducted to investigate the compositional evolution of the SEI layers on cycled anodes. At the surface level, the C 1s spectra showed typical peaks at 284.8 eV (C–C/C–H), 285.7 eV (C–O), and 287.2 eV (COO), while the O 1s spectra exhibited signals attributed to hydroxyl/ether (533.5 eV) and carbonyl groups (532.5 eV), confirming the presence of DME-derived organic species (Fig. 5a and Fig. S16a, b). Distinct peaks at 289.8 eV (CO_3^{2-}), 531.7 eV (Na–O), and 685.1 eV (Na–F) in the C 1s, O 1s, and F 1s spectra, respectively, indicate the presence of Na_2CO_3, Na_2O, and NaF (Fig. 5b).[58] Fluorinated species, including $-CF_2$ (689.0 eV) and NaF (685.1 eV), persisted even after extended sputtering, suggesting a spatially uniform distribution and high depth stability. Quantitative depth profiling revealed that the SEI on FR-HC contained approximately 40% less organic content than that on HC, implying suppressed solvent decomposition (Fig. S16c and d). After 45 s of sputtering, the SEI on FR-HC contained more than 70% inorganic species, with NaF as the dominant component, markedly exceeding the proportion observed in HC (<50%) (Fig. S16e). The inorganic-rich SEI architecture likely reduces interfacial ion transport resistance and limits parasitic side reactions, thereby promoting Na^+ migration and resulting in an obvious enhancement in the rate capability of FR-HC.[59,60]

In situ Raman spectroscopy was employed to track the structural evolution of FR-HC during electrochemical cycling (Fig. 5e and f). During discharging from the open-circuit voltage to 0.7 V, the D band gradually attenuated and broadened without a significant peak shift, suggesting Na^+ adsorption at defect sites and pore surfaces, which perturbs the vibrational modes of disordered carbon domains.[61] In the range of 0.7–0.1 V, a continued decline in D-band intensity was observed, accompanied by a noticeable blueshift in the G band. Such evolution reflects lattice distortion induced by SEI formation and partial Na^+ intercalation into SEI-derived amorphous carbon. Importantly, the simultaneous suppression of defect-related vibrational activity suggests that the SEI-derived graphitic coatings effectively alleviate the "trap effect" of structural defects, facilitating more homogeneous Na^+ accommodation. Upon further potential reduction below 0.1 V, the G band experienced accelerated attenuation, pronounced broadening, and continued blueshift, indicating deep Na^+ insertion into sp^2 carbon domains through a pore-filling behavior.[62] Notably, both D and G bands fully recovered during the charging process, confirming the excellent structural reversibility of FR-HC.

To visually evaluate the formation and reversibility of quasi-metallic Na clusters during cycling, a phenolphthalein-based chromogenic assay was employed (Fig. 5g). Upon immersing the discharged anodes in a 1 wt% phenolphthalein-ethanol solution, reactive sodium created localized alkalinity, triggering a distinct color change in the solution. As the discharge voltage decreased from 0.1 V (point c) to 0.01 V (point e), the solution color intensified from pale pink to deep purple, suggesting progressively enhanced quasi-metallic Na cluster formation within closed carbon pores. Notably, the strongest

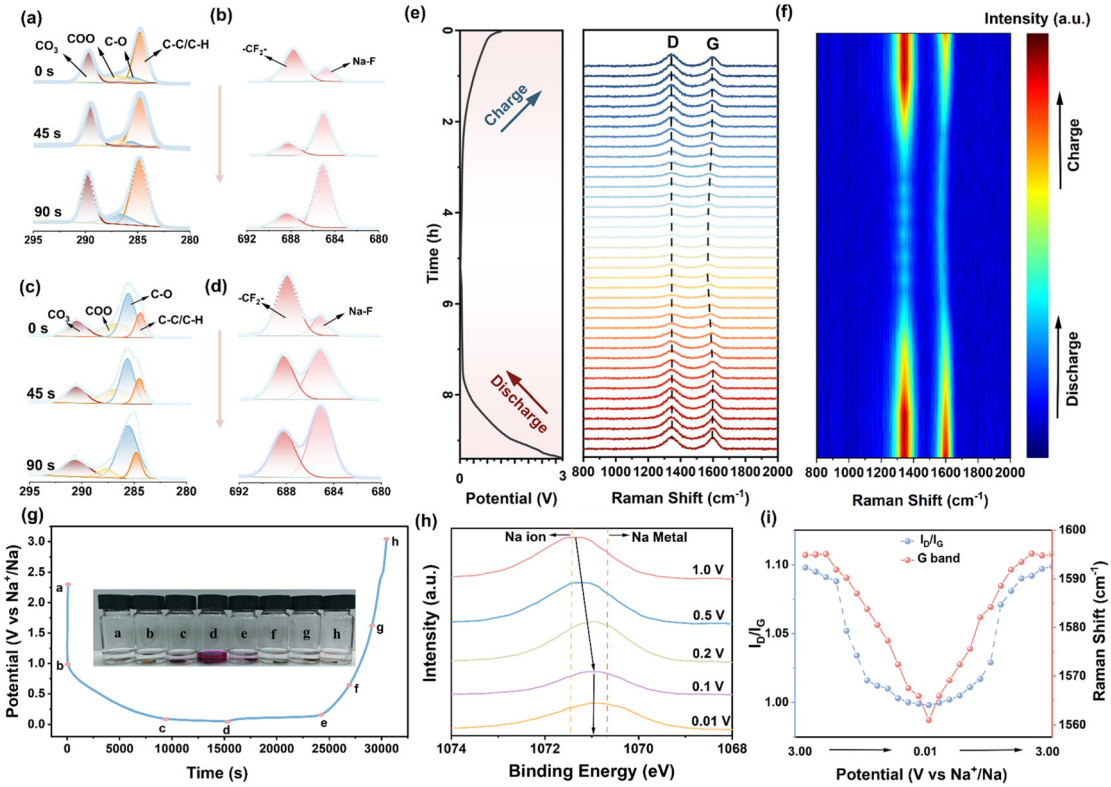

Fig. 5 Sputtered XPS C 1s spectra of FR-HC (a) and HC (c) electrodes. Sputtered XPS F 1s spectra of FR-HC (b) and HC (d) electrodes. (e) *In situ* Raman spectra of FR-HC and the corresponding charge/discharge profile at 50 mA g^{-1}. (f) Contour map of *in situ* Raman spectra. (g) Phenolphthalein-based chromogenic assays of FR-HC electrodes at different voltages. (h) *Ex situ* XPS spectra (Na 1s) of FR-HC at various discharge potentials. (i) Raman G-band shifts and I_D/I_G evolution with different potentials.

coloration occurred at 0.01 V (point e), indicating that pore-filling dominates the Na^+ storage mechanism in this voltage range. During the subsequent charging process, the coloration gradually faded and fully disappeared at 1.5 V (point h), indicating the reversible conversion of Na clusters back to ionic Na^+. These observations confirm a dendrite-free, confined Na storage process enabled by the structural design of FR-HC.

Ex situ XPS analysis of Na 1s through sodiation was carried out to further investigate the sodium storage behavior of FR-HC (Fig. 5h). At 0.1 V, a distinct shoulder appeared at a binding energy close to that of metallic Na, which can be attributed to the formation of C–Na interactions and quasi-metallic Na clusters confined within the carbon matrix. When the potential decreased to 0.01 V, the peak position remained unchanged, without shifting toward the standard binding energy of bulk metallic Na (~1071.8 eV), indicating that the confined environment stabilizes sodium clusters in a potential-independent manner. Notably, no signal corresponding to free metallic Na was detected throughout the 0.1–0.01 V discharge range, confirming that Na^+ is stored in a highly dispersed and trapped state rather than undergoing electrochemical plating. This confinement-governed Na storage process, devoid of metallic plating or dendritic formation, is conducive to structural integrity and long-term cycling stability.

To evaluate the practical electrochemical performance, sodium-ion full cells and pouch cells were assembled employing FR-HC as the anode and $NaNi_{1/3}Fe_{1/3}Mn_{1/3}O_2$ (NFM) as the cathode (Fig. 6a). Within the operating voltage window of 1.8–3.8 V, the FR-HC anode exhibited a pronounced low-potential plateau, which is beneficial for enhancing the overall energy density of the full-cell configuration (Fig. 6b). The rate capability assessment revealed outstanding reversible capacities of 158.7 mAh g^{-1} at 0.05 A g^{-1}, 146.3 mAh g^{-1} at 0.1 A g^{-1}, 136.6 mAh g^{-1} at 0.2 A g^{-1}, 122.8 mAh g^{-1} at 0.5 A g^{-1}, and 111.7 mAh g^{-1} at 1 A g^{-1} (Fig. 6c). The capacity loss at a high current density of 1 A g^{-1} remained below 15%, evidencing the rapid Na^+ transport kinetics and mechanical robustness of the FR-HC anode. To further validate practical feasibility, a soft-package pouch cell was fabricated with a cathode loading of 3.54 mg cm^{-2}. The device demonstrated excellent cycling stability, retaining 93% of its initial capacity after 100 cycles at 0.1 A g^{-1} (Fig. 6d), and exhibited remarkable high-rate capability, delivering 67.2 mAh g^{-1} even at 2 A g^{-1} (Fig. 6e). Significantly, the FR-HC//NFM pouch cell was capable of powering a 5 V miniature fan labeled "IFE" (Fig. 6f), thereby providing direct evidence of its applicability in real-device scenarios. Collectively, these findings demonstrate that FR-HC is a promising and scalable anode candidate for next-generation SIB systems with industrial relevance.

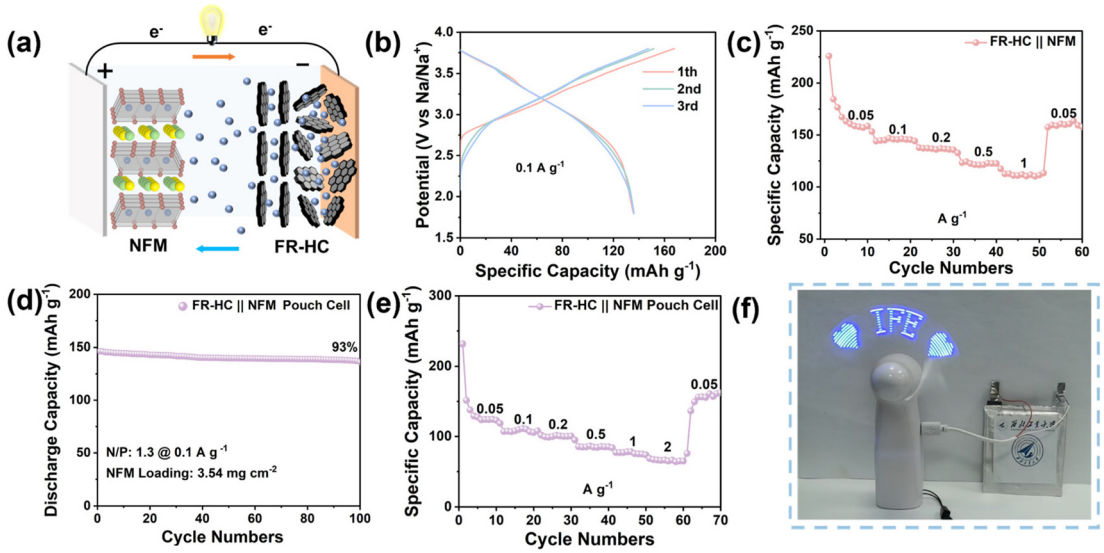

Fig. 6 (a) Schematic of a full cell configuration: an FR-HC anode paired with the $NaNi_{1/3}Fe_{1/3}Mn_{1/3}O_2$ (NFM) cathode. (b) Charge–discharge profiles of the full cell compared to a half cell. (c) Rate performance of the FR-HC//NFM full cell. (d) Cycling performance of the FR-HC//NFM pouch cell. (e) Rate capability of the FR-HC//NFM pouch cell. (f) Demonstration: a fan powered by the FR-HC//NFM pouch cell.

4. Conclusion

In summary, FJH enables the rapid regeneration of spent HC anodes within seconds, achieving simultaneous defect healing, graphitic ordering, and closed-pore reconstruction. During the ultrafast electrothermal process, a SEI-derived carbon coating is *in situ* formed and tightly bonded to the carbon surface, which effectively passivates structural defects and mitigates Na^+-trapping effects by providing uniform potential distribution and continuous electronic/ionic pathways. Meanwhile, the reconstructed interface promotes the formation of a new SEI enriched with inorganic components such as NaF, further enhancing interfacial stability and suppressing parasitic reactions. Benefiting from these coupled effects, the regenerated HC delivers a high ICE of 81% and outstanding rate capability, maintaining a distinct plateau capacity distribution even at 5 A g^{-1}. Beyond performance restoration, the FJH regeneration strategy aligns with key green chemistry principles, including energy efficiency, solvent elimination, process intensification, and waste minimization. These attributes highlight the potential of FJH as a sustainable direct regeneration pathway for HC anodes, providing a foundation for future system-level environmental assessments.

Conflicts of interest

There are no conflicts to declare.

Data availability

We declare that the data supporting the findings of this study are available within the article and its supplementary information (SI). The supplementary information contains additional experimental details, supporting characterization data, and supplementary electrochemical measurements. See DOI: https://doi.org/10.1039/d5gc06238a.

Additional raw data underlying the results of this study, if required in alternative formats, are available from the corresponding author upon reasonable request.

References

1 A. Yao, S. M. Benson and W. C. Chueh, *Nat. Energy*, 2025, **10**, 404–416.
2 Y. Zhao, Y. Kang, J. Wozny, J. Lu, H. Du, C. Li, T. Li, F. Kang, N. Tavajohi and B. Li, *Nat. Rev. Mater.*, 2023, **8**, 623–634.
3 Z. Cui, C. Liu and A. Manthiram, *Adv. Mater.*, 2025, 2420463.
4 H. Yang, D. Wang, Y. Liu, Y. Liu, B. Zhong, Y. Song, Q. Kong, Z. Wu and X. Guo, *Energy Environ. Sci.*, 2024, **17**, 1756–1780.
5 H. Rostami, J. Valio, P. Suominen, P. Tynjälä and U. Lassi, *Chem. Eng. J.*, 2024, **495**, 153471.
6 Y. Hao, J. Guo, W. Liu, X. Zhou, Z. Tian, Z. Zhang, Y. Li, X. Zhang and Y. Jiang, *ACS Nano*, 2025, **19**, 4496–4504.
7 R. Zhang, J. Liang, C. Zeng, J. Chen, Y. Ma, T. Zhai and H. Li, *Sci. China Mater.*, 2023, **66**, 88–96.
8 P. Ge, B. Wang, C. Zhu, H. Lei, H. Zhou, W. Sun, X. Ji and Y. Yang, *Adv. Energy Mater.*, 2025, **15**, e03677.
9 Y. Pi, J. Xiao, Y. Liu, K. Feng, L. Xiong, J. Liu, F. Wang, C. Dong, Y. Ding and X. Xu, *J. Energy Storage*, 2025, **113**, 115593.
10 X. Fan, X. Kong, P. Zhang and J. Wang, *Energy Storage Mater.*, 2024, **69**, 103386.

11 S. Sharma, V. Manchala, R. Gopalan, T. N. Rao and B. Das, *Carbon*, 2024, **226**, 119158.
12 X. Zhao, P. Shi, H. Wang, Q. Meng, X. Qi, G. Ai, F. Xie, X. Rong, Y. Xiong, Y. Lu and Y.-S. Hu, *Energy Storage Mater.*, 2024, **70**, 103543.
13 Z. Zhou, Z. Wang, Y. Zhang, Q. Lin, Y. Shuai and L. Fan, *Energy Storage Mater.*, 2025, **80**, 104443.
14 C. Vaalma, D. Buchholz, M. Weil and S. Passerini, *Nat. Rev. Mater.*, 2018, **3**, 18013.
15 S. Gan, Y. Huang, N. Hong, Y. Zhang, B. Xiong, Z. Zheng, Z. He, S. Gao, W. Deng, G. Zou, H. Hou and X. Ji, *Nano-Micro Lett.*, 2025, **17**, 325.
16 Z. Tang, R. Zhang, H. Wang, S. Zhou, Z. Pan, Y. Huang, D. Sun, Y. Tang, X. Ji, K. Amine and M. Shao, *Nat. Commun.*, 2023, **14**, 6024.
17 T. W. Surta, E. Koh, Z. Li, D. B. Fast, X. Ji, P. A. Greaney and M. R. Dolgos, *Adv. Energy Mater.*, 2022, **12**, 2200647.
18 D. Sun, B. Luo, H. Wang, Y. Tang, X. Ji and L. Wang, *Nano Energy*, 2019, **64**, 103937.
19 Y. Yang, C. Wu, X.-X. He, J. Zhao, Z. Yang, L. Li, X. Wu, L. Li and S.-L. Chou, *Adv. Funct. Mater.*, 2024, **34**, 2302277.
20 R. Qiu, D. Ma, H. Zheng, M. Liu, J. Cai, W. Yan and J. Zhang, *Nano Energy*, 2024, **128**, 109920.
21 J. Pan, Y.-Y. Sun, Y. Yan, L. Feng, Y. Zhang, A. Lin, F. Huang and J. Yang, *JACS Au*, 2021, **1**, 1208–1216.
22 K. Li, J. Zhang, D. Lin, D.-W. Wang, B. Li, W. Lv, S. Sun, Y.-B. He, F. Kang, Q.-H. Yang, L. Zhou and T.-Y. Zhang, *Nat. Commun.*, 2019, **10**, 725.
23 Y. Huang, L. Zhao, L. Li, M. Xie, F. Wu and R. Chen, *Adv. Mater.*, 2019, **31**, 1808393.
24 W. Chen, R. V. Salvatierra, J. T. Li, C. Kittrell, J. L. Beckham, K. M. Wyss, N. La, P. E. Savas, C. Ge, P. A. Advincula, P. Scotland, L. Eddy, B. Deng, Z. Yuan and J. M. Tour, *Adv. Mater.*, 2023, **35**, 2207303.
25 Z. Zhang, X. Zhu, H. Hou, L. Tang, J. Xiao and Q. Zhong, *Waste Manage.*, 2022, **150**, 30–38.
26 Z. Geng, J. Liu, Y. Geng, M. Peng, M. Xiong, H. Shi and X. Luo, *New J. Chem.*, 2022, **46**, 20250–20259.
27 Q. Chen, L. Huang, J. Liu, Y. Luo and Y. Chen, *Carbon*, 2022, **189**, 293–304.
28 C. Yi, P. Ge, X. Wu, W. Sun and Y. Yang, *J. Energy Chem.*, 2022, **72**, 97–107.
29 Y. Hou, H. Guo, B. Xing, H. Zeng, W. Kang, X. Qu, C. Zhang, J. Jia, G. Huang and Y. Cao, *Fuel*, 2024, **374**, 132488.
30 Y. Lei, J. Zhang, X. Chen, W. Min, R. Wang, M. Yan and J. Xu, *Mater. Today Energy*, 2022, **26**, 100997.
31 N. Yao, F. Liu, Y. Zou, H. Wang, M. Zhang, X. Tang, Z. Wang, M. Bai, T. Liu, W. Zhao, R. Xue, Y. Liu and Y. Ma, *Energy Storage Mater.*, 2023, **55**, 417–425.
32 L. Eddy, S. Xu, C. Liu, P. Scotland, W. Chen, J. L. Beckham, B. Damasceno, C. H. Choi, K. Silva, A. Lathem, Y. Han, B. I. Yakobson, X. Zhang, Y. Zhao and J. M. Tour, *J. Am. Chem. Soc.*, 2024, **146**, 16010–16019.
33 K. M. Wyss, D. X. Luong and J. M. Tour, *Adv. Mater.*, 2022, **34**, 2106970.
34 P. Huang, R. Zhu, X. Zhang and W. Zhang, *Chem. Eng. J.*, 2022, **450**, 137999.
35 S. Molina-Molina, A. Perejón, L. A. Pérez-Maqueda and P. E. Sánchez-Jiménez, *Scr. Mater.*, 2024, **247**, 116086.
36 J. Yuan, Y. Zhang, F. Chen and Z. Gu, *J. Mater. Chem. C*, 2024, **12**, 14729–14753.
37 M. Shan, S. Xu, Y. Cao, B. Han, X. Zhu, T. Zhang, C. Dang, J. Zhu, Q. Zhou, Z. Xue, Y. Xu, Q. Zhu, M. S. Islam, B. H. Yin, X. Chang, C. Cao, G. Xu and M. Zhu, *Adv. Funct. Mater.*, 2024, **34**, 2411834.
38 W. Chen, J. Chen, K. V. Bets, R. V. Salvatierra, K. M. Wyss, G. Gao, C. H. Choi, B. Deng, X. Wang, J. T. Li, C. Kittrell, N. La, L. Eddy, P. Scotland, Y. Cheng, S. Xu, B. Li, M. B. Tomson, Y. Han, B. I. Yakobson and J. M. Tour, *Sci. Adv.*, 2023, **9**, eadh5131.
39 T. Li, L. Tao, L. Xu, T. Meng, B. C. Clifford, S. Li, X. Zhao, J. Rao, F. Lin and L. Hu, *Adv. Funct. Mater.*, 2023, **33**, 2302951.
40 S. Dong, Y. Song, K. Ye, J. Yan, G. Wang, K. Zhu and D. Cao, *EcoMat*, 2022, **4**, e12212.
41 H. Yu, M. Huang, Y. Li, L. Chen, H. Lv, L. Yang and X. Luo, *J. Energy Chem.*, 2025, **105**, 501–513.
42 A. Shen, J. Zhang, Y. Chen and C. Wang, *Resour., Conserv. Recycl.*, 2025, **222**, 108433.
43 C. Li, P. Kou, H. Wen, Y. Zhou, X. Gao and Y. Mi, *J. Alloys Compd.*, 2024, **990**, 174446.
44 J. Song, B. Xiao, Y. Lin, K. Xu and X. Li, *Adv. Energy Mater.*, 2018, **8**, 1703082.
45 Y. Li, F. Wu, Y. Li, M. Liu, X. Feng, Y. Bai and C. Wu, *Chem. Soc. Rev.*, 2022, **51**, 4484–4536.
46 S. Dong, Y. Song, Y. Fang, G. Wang, Y. Gao, K. Zhu and D. Cao, *ACS Appl. Energy Mater.*, 2024, **7**, 11288–11296.
47 J. Liu, Y. You, L. Huang, Q. Zheng, Z. Sun, K. Fang, L. Sha, M. Liu, X. Zhan, J. Zhao, Y.-C. Han, Q. Zhang, Y. Chen, S. Wu and L. Zhang, *Adv. Mater.*, 2024, **36**, 2407369.
48 J. He, Y. Zhao, Y. Li, Q. Yuan, Y. Wu, K. Wang, K. Sun, J. Wu, J. Jiang, B. Zhang, L. Wang and M. Fan, *Nano-Micro Lett.*, 2025, **17**, 1–16.
49 Q. Li, X. Liu, Y. Tao, J. Huang, J. Zhang, C. Yang, Y. Zhang, S. Zhang, Y. Jia, Q. Lin, Y. Xiang, J. Cheng, W. Lv, F. Kang, Y. Yang and Q.-H. Yang, *Natl. Sci. Rev.*, 2022, **9**, nwac084.
50 Y. Qiu, Y. Su, X. Jing, H. Xiong, D. Weng, J. G. Wang, F. Xu and H. Wang, *Adv. Funct. Mater.*, 2025, **35**, 2423559.
51 P. Huang, Z. Guo, Z. Li, L. Chen, W.-D. Liu, J. Luo, Z. Liu, J. Zhang, J. Zeng, W. Zhang, X. Zhang, R. Zhu and Y. Chen, *Adv. Mater.*, 2025, **37**, 2507521.
52 X. Huo, G. Gao, B. Li, Z. Zhou, K. Shu, J. Bi, Z. Du, L. Xu and W. Ai, *Adv. Energy Mater.*, 2025, **15**, 2502238.
53 X. Yi, X. Li, J. Zhong, S. Wang, Z. Wang, H. Guo, J. Wang and G. Yan, *Adv. Funct. Mater.*, 2022, **32**, 2209523.
54 C. Wu, Y. Yang, Y. Li, X. He, Y. Zhang, W. Huang, Q. Chen, X. Liu, S. Chen, Q. Gu, L. Li, S. C. Smith, X. Tan, Y. Yu, X. Wu and S. Chou, *Energy Environ. Sci.*, 2025, **18**, 6019–6031.

55 K. Wang, M. Li, Z. Zhu, W. Ai, H. Wu, B. Wang, P. He, D. Xie, J. Wu and W. Huang, *Nano Energy*, 2024, **124**, 109459.
56 Z. Tang, D. Jiang, Z. Fu, J. Zhou, R. Liu, R. Zhang, D. Sun, A. S. Dhmees, Y. Tang and H. Wang, *Small Methods*, 2024, **8**, 2400509.
57 Y. Lu, C.-Z. Zhao, J.-Q. Huang and Q. Zhang, *Joule*, 2022, **6**, 1172–1198.
58 Z. Lv, T. Li, X. Hou, C. Wang, H. Zhang, J. Yan, Q. Zheng and X. Li, *Chem. Eng. J.*, 2022, **430**, 133143.
59 Z. Tang, H. Wang, P.-F. Wu, S.-Y. Zhou, Y.-C. Huang, R. Zhang, D. Sun, Y.-G. Tang and H.-Y. Wang, *Angew. Chem., Int. Ed.*, 2022, **61**, e202200475.
60 M. Liu, F. Wu, Y. Gong, Y. Li, Y. Li, X. Feng, Q. Li, C. Wu and Y. Bai, *Adv. Mater.*, 2023, **35**, 2300002.
61 C. Wu, Y. Yang, Y. Zhang, H. Xu, W. Huang, X. He, Q. Chen, H. Dong, L. Li, X. Wu and S. Chou, *Angew. Chem., Int. Ed.*, 2024, **63**, e202406889.
62 Y. Wei, X. Ji, Z. Lu, H. Jin, X. Kong, S. Jin and H. Ji, *Adv. Funct. Mater.*, 2024, **34**, 2315408.